Dynamic Regimes for Driven Colloidal Particles on a Periodic Substrate at Commensurate and Incommensurate Fillings

D. McDermott[1,2], J. Amelang[1,3], C. J. Olson Reichhardt[1], and C. Reichhardt[1]
[1] *Theoretical Division, Los Alamos National Laboratory, Los Alamos, New Mexico 87545 USA*
[2] *Department of Physics, University of Notre Dame, Notre Dame, Indiana 46556 USA*
[3] *Division of Engineering and Applied Science, California Institute of Technology, Pasadena, California 91125 USA*
(Dated: June 10, 2013)

We examine colloidal particles driven over a periodic muffin tin substrate using numerical simulations. In the absence of a driving force this system exhibits a rich variety of commensurate and incommensurate static phases in which topological defects can form domain walls, ordered stripes, superlattices, and disordered patchy regimes as a function of the filling fraction. When an external drive is applied, these different static phases generate distinct dynamical responses. At incommensurate fillings the flow generally occurs in the form of localized pulses or solitons correlated with the motion of the topological defect structures. We also find dynamic transitions between different types of moving states that are associated with changes in the velocity force curves, structural transitions in the topological defect arrangements, and modifications of the velocity distributions and particle trajectories. We find that the dynamic transitions between ordered and disordered flows exhibit hysteresis, while in strongly disordered regimes there is no hysteresis and the velocity force curves are smooth. When stripe patterns are present, transport can occur along the stripe direction rather than along the driving direction. Structural dynamic transitions can also occur within the pinned regimes when the applied drive causes distortions of the interstitially pinned particles while the particles trapped at pinning sites remain immobile.

PACS numbers: 82.70.Dd,83.80.Hj

I. INTRODUCTION

Non-driven systems of collectively interacting particles typically form some type of crystal structure that is generally triangular for repulsively interacting particles confined to two dimensions (2D). In the presence of a periodic substrate, the particles adjust their positions according to the periodicity and strength of the substrate. If the particle lattice and substrate periodicities match, an ordered commensurate state forms. Similar commensurate conditions may recur for higher integer filling factors $f = n/m$, where n is the number of particles and m is the number of substrate minima. When the particle lattice and substrate periodicities do not match, the system is incommensurate[1], and the particles may sit mostly in an integer matching configuration with isolated spots of extra or missing particles, or the system may break up into domains[2–4]. If an external drive is applied to the particles, the depinning threshold and dynamic response depend strongly on the filling fraction and whether the configuration is commensurate or incommensurate. Specific examples of systems that exhibit commensurate-incommensurate transitions connected to depinning and sliding dynamics include vortices in type-II superconductors interacting with nanostructured periodic pinning arrays[5–10], vortices in Bose-Einstein condensates with a co-rotating periodic optical trap array[11], charge density wave systems[12], colloidal particles on periodic substrates[13–22], charged metallic balls on patterned surfaces[23], and frictional systems[24–31].

One system that has recently attracted attention as an ideal model for studying the dynamics of commensurate-incommensurate behavior is repulsively interacting colloidal particles confined by a periodic substrate. Experiments and computational studies have shown that a variety of colloidal orderings can arise for colloidal particles interacting with one dimensional (1D) periodic substrates[13,32,33], 2D periodic substrates[15,20,21,34–38], 2D quasiperiodic substrates[42,43,45,46] or 2D random substrates[39]. While these studies have provided a better understanding of the general features of commensurate-incommensurate behaviors, being able to *control* colloidal ordering and colloidal dynamics would lead to a variety of applications including self-assembled structures, particle separation, and photonic crystals.

In recent experiments, velocity versus applied force curves were obtained for an assembly of colloidal particles driven over a periodic substrate[40]. These experiments showed that the largest depinning threshold occurs for the commensurate state at which there is one colloid per substrate minimum. At incommensurate fillings, the depinning threshold is substantially reduced and the flow occurs through localized soliton type pulse motions, where individual particles do not move continuously through the sample but instead jump by one lattice constant each time the soliton or kink moves past. Just above the first matching filling, a forward-moving kink forms, while just below the first matching filling, there is a backward-moving anti-kink or vacancy. In both cases the net motion of the particles is in the forward direction. At the commensurate filling, a kink-antikink pair can be created, so that even for commensurate states the motion can consist of temporarily mobile particles co-existing with pinned particles. Subsequent numerical simulations of Yukawa particles inter-

acting with egg-carton substrates also produced kink and antikink motion, which the authors related to an effective friction[21,38]. These works showed that decreasing the substrate strength at an incommensurate filling leads to a 2D Aubry transition[41], where the depinning threshold vanishes and the colloidal lattice essentially floats on the substrate. In addition, the velocity force curves exhibited signatures of two step depinning processes corresponding to the different dynamical states of soliton depinning and the depinning of all of the particles. Soliton-type flow for driven particle systems has also been studied for friction models[25–27] as well as for vortices in type-II superconductors interacting with periodic pinning arrays, where the soliton flow produces distinct features in the current-voltage curves that are analogs to the velocity-force curves in the driven colloidal systems[8–10,47]. In numerical[42] and experimental[44] studies of the driven dynamics of colloidal particles moving over periodic substrates, different dynamical locking regimes and dynamical ordering were observed. Here, the type of motion and amount of order in the flow depends on the orientation of the driving direction with respect to the symmetry directions of the substrate. Kink motion has also been found in experiments on colloidal particles moving over quasiperiodic substrates[45]. In addition, in studies of colloidal particles driven over corrugated 1D arrays, different dynamical transitions between pinned, smectic and disordered flowing regimes were observed[33].

The recent experiments on the dynamics of colloidal particles sliding over periodic arrays focused only on fillings very near the first matching condition[40]. For higher fillings or other types of periodic substrates, an additional variety of dynamical phases should be expected to appear. In a recent study[4] we described the pinned configurations for colloidal particles interacting with a 2D square periodic array of pinning sites for fillings ranging from $f = 1.0$ to 9.0. We particularly focused on the regime between $f = 4.0$ and $f = 5.0$ since it contains a transition from a triangular colloidal lattice at $f = 4.0$ to a square lattice at $f = 5.0$. The system forms domain walls composed of topological defects for incommensurate fillings just above and below $f = 4.0$, transitions to stripe patterns for $4.1 < f < 4.6$, and exhibits disordered patchy domains for $4.6 < f < 5.0$. The periodic substrate in Ref.[4] is not an egg carton potential of the type used in the recent driven colloidal experiments[40] or in static ordering studies for colloidal particles in 2D arrays[14,15,20], but is instead a muffin tin structure formed from a periodic array of localized pinning sites with small radii, so that beyond $f = 1.0$ the additional colloidal particles sit in the interstitial regions between the particles that are trapped directly by the pinning sites. Periodic pinning arrangements of this type have been experimentally realized in colloidal systems and studied in the range $f = 4.0$ to $f = 5.5$, with a triangular colloidal lattice observed at $f = 4.0$ when the pinning strength was such that each pinning site captures only one particle[48]. Such pinning arrays have also been used to study dynamical locking for colloidal particles driven over a substrate at different angles with respect to the substrate symmetry directions[34]. Experimental and numerical studies of vortex systems using similar 2D periodic pinning arrays also obtained a triangular vortex lattice at $f = 4.0$ and a square lattice at $f = 5.0$[5,7] with domain wall and stripe states between these fillings[5]. Since the static phases have already been characterized, colloidal particles interacting with a muffin tin potential may be an ideal system for understanding how depinning dynamics occurs in the presence of domain walls or stripes, or in systems with coexisting ordered and disordered phases.

II. SIMULATION AND SYSTEM

Our system consists of a 2D assembly of colloidal particles that interact repulsively via a Yukawa potential. The initial configurations of the N_c particles are obtained using a simulated annealing procedure. After annealing, we apply an external drive $\mathbf{F}^D = F_d\hat{\mathbf{x}}$ to each particle. The system has periodic boundary conditions in both the x and y directions. The dynamics of the particles is obtained by using an overdamped equation of motion, as in previous numerical studies[4,14,20,42]. The motion of a single particle i is given by integrating the following equation:

$$\eta\frac{d\mathbf{R}_i}{dt} = -\sum_{i\neq j}^{N_i}\nabla V(R_{ij}) + \mathbf{F}_i^P + \mathbf{F}^D + \mathbf{F}_i^T. \qquad (1)$$

Here η is the damping constant and the particle-particle interaction potential is $V(R_{ij}) = q^2E_0\exp(-\kappa R_{ij})/R_{ij}$, where $E_0 = Z^{*2}/4\pi\epsilon\epsilon_0 a_0$, q is the dimensionless interaction strength, Z^* is the effective charge of the colloid, and ϵ is the solvent dielectric constant. The screening length is $1/\kappa$ and the lengths are measured in units of a_0, time in units of $\tau = \eta/E_0$, and forces in units of $F_0 = E_0/a_0$. $\mathbf{R}_{i(j)}$ is the position of particle $i(j)$, and $R_{ij} = |\mathbf{R}_i - \mathbf{R}_j|$. The substrate is modeled as N_p pinning sites placed in a square array with a lattice constant a. Each pinning site is represented by a parabolic potential trap with a radius $R_p = 0.3a_0$ which gives rise to a pinning force of $\mathbf{F}_i^P = \sum_{k=1}^{N_p} F_p(R_{ik}/R_p)\Theta(R_p - R_{ik})\hat{\mathbf{R}}_{ik}$, where $R_{ik} = |\mathbf{R}_i - \mathbf{R}_k|$ is the distance between particle i and the center of pinning site k, and $\hat{\mathbf{R}}_{ik} = (\mathbf{R}_i - \mathbf{R}_k)/R_{ik}$. $F_p = 10$ is the maximum force of the pinning site, and Θ is the Heaviside step function. The thermal fluctuations come from the Langevin noise term F^T with the properties $\langle F^T(t)\rangle = 0$ and $\langle F_i^T(t)F_j^T(t')\rangle = 2\eta k_BT\delta_{ij}\delta(t-t')$, where k_B is the Boltzmann constant.

After annealing, we set $T = 0$ and begin applying a drive by starting at $F_d = 0$ and increasing F_d in steps of $\delta F_d = 0.001$, waiting 5×10^4 simulation time steps at each force increment. We have tested the results for slower drive sweep rates and find that they do not change. We measure the average particle velocity

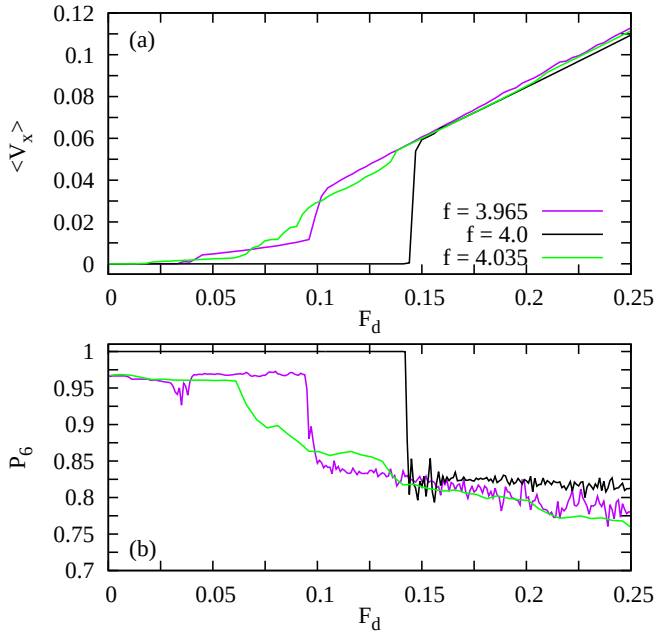

FIG. 1: (a) The average velocity $\langle V_x \rangle$ vs F_d for a filling of $f = 4.0$ (black), $f = 3.965$ (purple), and $f = 4.035$ (green). (b) The corresponding fraction of six-fold coordinated particles P_6 vs F_d.

$\langle V_x \rangle = N_c^{-1} \sum_{i=1}^{N_c} \mathbf{v}_i \cdot \hat{\mathbf{x}}$, and $\langle V_y \rangle = \sum_{i=1}^{N_c} \mathbf{v}_i \cdot \hat{\mathbf{y}}$. We also measure the distributions $P(v_x)$ and $P(v_y)$ of the instantaneous particle velocities in the x and y directions, respectively. The fraction of $n-$fold coordinated particles P_n is obtained using a Voronoi construction, with $P_n = \sum_i^{N_c} \delta(n - z_i)$, where z_i is the coordination number of particle i. The filling fraction is defined as $f = N_c/N_p$. In this study we consider the case where each pinning site captures at most one particle and limit our range of F_d such that particles trapped at pinning sites do not depin, so that we can concentrate on the initial flow of the particles trapped in the interstitial regions.

III. FILLINGS NEAR $f = 4.0$

At $f = 4.0$, we previously found that the non-driven colloidal configuration is a triangular lattice, while for $3.9 < f < 4.0$ and $4.0 < f < 4.1$, the same triangular lattice is interspersed with grain boundaries of 5-7 paired dislocations separating regions where the particle lattice is rotated with respect to the substrate[4]. In Fig. 1(a) we plot $\langle V_x \rangle$ versus F_d for samples with $f = 3.965$, 4.0, and 4.035, and in Fig. 1(b) we plot the corresponding fraction of sixfold coordinated particles P_6. At the commensurate filling of $f = 4.0$, there is a finite depinning threshold near $F_d = 0.14$, while for the incommensurate fillings, the depinning threshold is almost zero for $f = 4.035$ and slightly higher than zero for $f = 3.965$. The velocity force curves at the incommensurate fillings show a multiple depinning response as indicated by the multiple jumps in $\langle V_x \rangle$. In Fig. 1(b), $P_6 = 1.0$ for the $f = 4.0$ system for drives below the depinning threshold due to the triangular ordering of the pinned state, but P_6 drops at depinning when only the interstitially pinned particles are able to move, causing some non-sixfold ordering to appear. For the $f = 4.035$ sample, initially $P_6 < 1.0$ since the particles in the grain boundaries are $5-$ or $7-$fold coordinated, and for $F_d > 0.06$, P_6 drops further since more non-sixfold coordinated defects are generated as F_d increases.

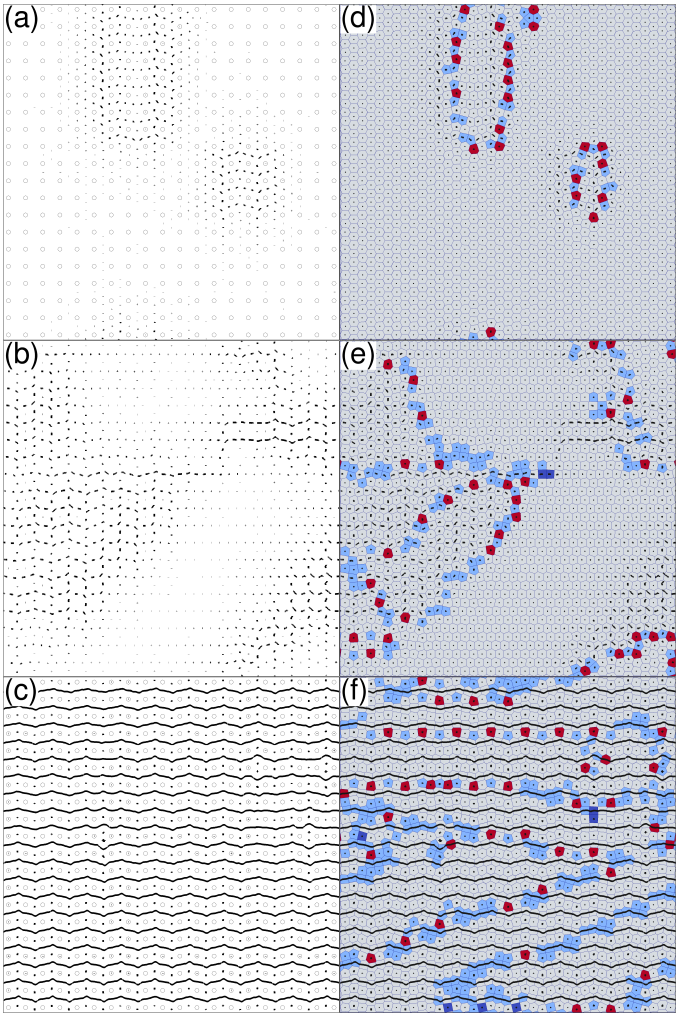

FIG. 2: (a-c) The pinning site locations (open circles) and particle trajectories (black lines) over a fixed interval of time for the system at $f = 4.035$. (a) $F_d = 0.05$, (b) $F_d = 0.08$, and (c) $F_d = 0.2$. (d-f) Pinning site locations (open circles), particle trajectories (black lines), and Voronoi construction (blue lines) for the same sample at (d) $F_d = 0.05$, (e) $F_d = 0.08$, and (f) $F_d = 0.2$. The Voronoi polygons are colored according to their number of sides: 4 (dark blue), 5 (light blue), 6 (white), and 7 (red). (a,d) The moving grain boundary state; (b,e) the fluctuating grain boundary state; and (c,f) the continuous flow regime.

It is the depinning of the grain boundaries that is responsible for reducing the depinning force at the incommensurate fillings. Above depinning at these fillings, the grain boundaries move continuously but the particles only move about a lattice constant each time a grain boundary passes over them. This is illustrated in Fig. 2(a) where we plot the particle trajectories over a fixed time for a sample with $f = 4.035$ at $F_d = 0.05$. The particle motion is localized and correlated with the positions of the grain boundaries, as shown by the corresponding Voronoi construction in Fig. 2(d); motion occurs only where the grain boundaries are located, while regions without grain boundaries remain pinned. When the particles move, their trajectories are not strictly 1D but have a zig-zag shape due to the fact that the particles must shift in both the x and y directions to permit the grain boundary to pass, since the particles change from one triangular lattice orientation to the other after the grain boundary has moved over them. This motion has similarities to the soliton or kink motion observed near the $f = 1.0$ filling in experiments and simulations[21,40], but instead of isolated moving kinks or antikinks, we have a moving row of correlated kinks or anti-kinks that is bound to the grain boundary. The shape of the moving domain that the grain boundary defines does not remain completely static but can undergo expansions and contractions as it moves.

For $F_d = 0.08$, we find a transition from well-defined domain walls to a state where the domain walls break apart and reform, as illustrated in Fig. 2(b). The motion still remains localized to the vicinity of the domain walls, as shown in Fig. 2(e). The domain wall number strongly fluctuates in this state, which resembles the kink-antikink nucleation regime observed in the experiments of Ref.[40]. At $F_d = 0.2$, the flow of the mobile particles is continuous, but a portion of the interstitially pinned particles, as well as all of the directly pinned particles, remain immobile. In this regime, the soliton motion is lost, as illustrated in Fig. 2(c). In addition, the grain boundary state is destroyed due to a proliferation of 5-fold and 7-fold coordinated particles, as shown in Fig. 2(f). At $f = 3.965$, where there is also a grain boundary pinned state, we find a sequence of dynamical states very similar to those shown in Fig. 2 for $f = 4.035$.

We can identify four distinct dynamical regimes for the grain boundary forming fillings: (I) pinned; (II) grain boundary motion; (III) moving fluctuating grain boundaries; and (IV) continuous interstitial flow. The different regimes can also be characterized with the distributions $P(v_x)$ and $P(v_y)$ of the instantaneous particle velocities, as shown for the $f = 4.035$ sample at $F_d = 0.05$ in Fig. 3(a). Here, in the moving grain boundary state, there is a peak in $P(v_x)$ at $v_x = 0.0$ from the immobile particles, a second peak near $v_x = 0.025$, and continuous weight between the two peaks. Although the grain boundaries move at constant speed, the individual particles start with $v_x = 0$ in the pinned state, reach a maximum velocity as the grain boundary moves past, and then drop back to the $v_x = 0$ pinned state. As a result, we observe the full range of velocities between $v_x = 0$ and $v_x = 0.025$. Fig. 3(d) shows that the y velocities of the particles at the same drive are not strictly zero due to the zig-zag motion associated with the grain boundaries; however, the average value of v_y is zero. For $F_d = 0.08$ in the same system, Fig. 3(b) shows that $P(v_x)$ is skewed out to higher positive v_x values than for the $F_d = 0.05$ case, but the secondary peak in $P(v_x)$ has disappeared due to the strongly fluctuating nature of the grain boundary motion in this regime. In the corresponding $P(v_y)$ shown in Fig. 3(e), the tails have moved out further in the positive and negative v_y directions. For $F_d = 0.20$ in the continuous flow regime, $P(v_x)$ in Fig. 3(c) has two distinct peaks with one centered at $v_x = 0.0$ and the other centered at $v_x = 0.16$. A region of zero weight exists between the two peaks, indicating that there are no particles moving at these intermediate velocities. This is due to the loss of the soliton-like motion; in the continuous flow regime, the mobile particles always remain in motion while the pinned particles always remain immobile. The corresponding $P(v_y)$ in Fig. 3(f) is still centered at zero but now shows additional structure with two satellite peaks that arise due to the sinuous motion in this regime, as illustrated in Fig. 2(c). For increasing F_d, $P(v_x)$ and $P(v_y)$ retain the same form shown in Fig. 3(c,f) until the particles at the pinning sites depin, upon which a new set of dynamical states appears that will not be considered in this work.

To test for hysteretic effects, we measure $P(v_x)$ and $P(v_y)$ both for increasing F_d up to its maximum value (black curves in Fig. 3) and for decreasing F_d back down to zero (filled red curves in Fig. 3). In the continuous flow regime, Fig. 3(c) shows that there is no hysteresis; however, in the moving fluctuating grain boundary regime [Fig. 3(b)] the system is generally more disordered when F_d is being decreased, indicating that the fluctuating grain boundary regime persists down to a lower drive on the downward sweep of F_d than the drive at which it first appeared during the upward sweep of F_d. Once the drive is low enough, the grain boundaries reform and the hysteresis is lost, as shown in Fig. 3(a).

For $f = 3.965$, a similar sequence of phases occur with similar characteristics in the velocity histograms; however, in this case the moving grain boundary regime persists up to higher drives. We find the same general features of the velocity histograms and dynamic phases for other fillings where grain boundary formation occurs in the pinned state. Such grain boundary states usually occur close to the integer fillings such as near $f = 3.0$ and $f = 4.0$.

A. Stripes and Symmetry Breaking Flows

At filling fractions where the topological defects form stripe structures, the system initially depins into a moving stripe phase, such as shown in Fig. 4(a) for $f = 4.3$

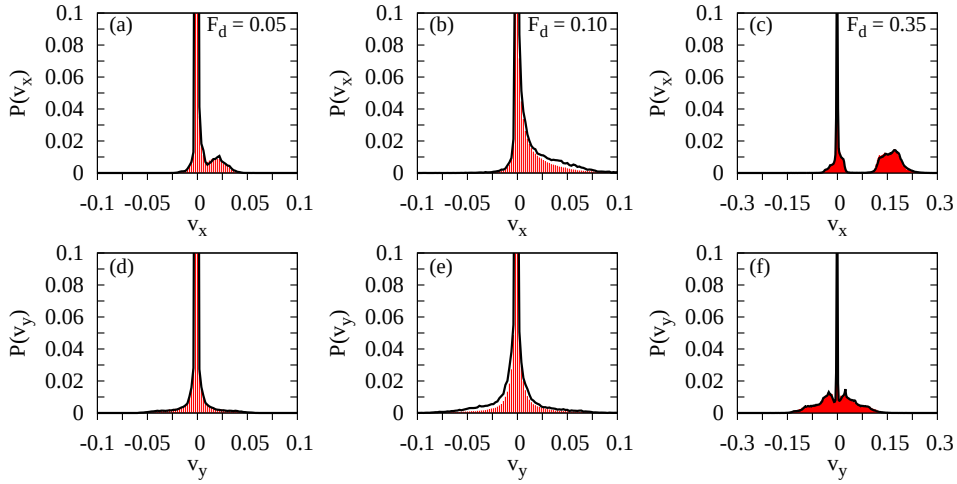

FIG. 3: The velocity histograms for the system in Fig. 2 with $f = 4.035$. (a,b,c) $P(v_x)$; (d,e,f) $P(v_y)$. (a,d) $F_d = 0.05$. (b,e) $F_d = 0.8$. (c,f) $F_d = 0.2$. Black lines: increasing sweep of F_d. Filled red curves: decreasing sweep of F_d.

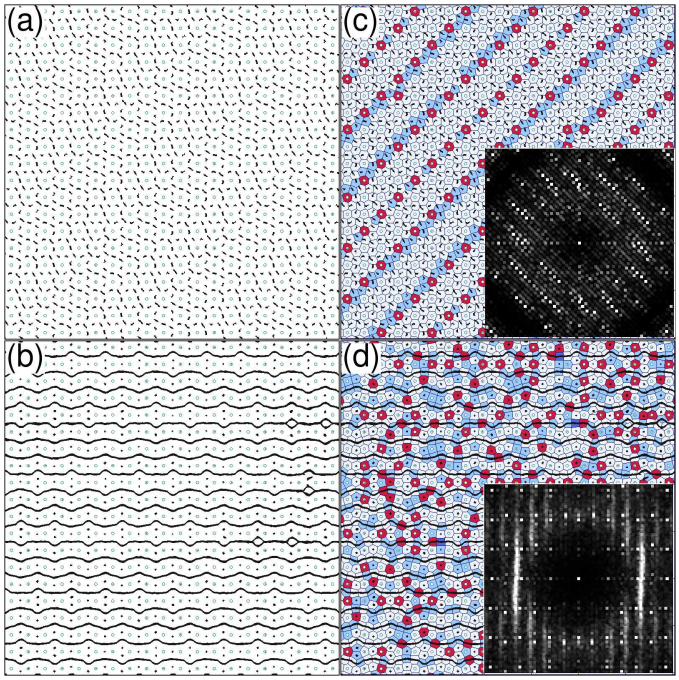

FIG. 4: The dynamics at f = 4.3, where the zero drive state forms a stripe pattern of topological defects. (a) The particle trajectories over time for the moving stripe state at $F_d = 0.05$ showing that the particles are not moving along the direction of the drive but are moving in the positive x and negative y directions. (b) The particle trajectories over time for the disordered flow state at $F_d = 0.035$, indicating that the particles form 1D channels of flow in the direction of the drive. (c) Voronoi construction (blue lines) of the moving stripe state in (a). Inset: the structure factor $S(k)$ indicates that the system is ordered. (d) Voronoi construction of the disordered flow state in (b). Inset: $S(k)$ shows that the sample has a smectic type ordering. The Voronoi polygons are colored according to their number of sides: 4 (dark blue), 5 (light blue), 6 (white), and 7 (red).

and $F_d = 0.05$. The moving state is highly ordered, as indicated by the structure factor $S(k)$ plotted in the inset of Fig. 4(c). At higher drives there is a transition to a state where the stripe structure breaks down and the system becomes more disordered, as shown in Fig. 4(c) for $F_d = 0.35$. In the inset of Fig. 4(c), the anisotropic features in $S(k)$ reveal that the system is more disordered with smectic ordering along the x-direction.

In the moving stripe phase, the particles do not flow along the x direction but instead move at an angle to the driving direction, as shown in Fig. 4(a) for the state in Fig. 4(c). Here the particles travel in both the positive x and negative y directions, while at $F_d = 0.35$, Fig. 4(b) indicates that the flow is now strictly in the x-direction. In the moving smectic phase at $F_d = 0.35$, the particles at the pinning sites and some of the interstitial particles are immobile, and the moving interstitial particles form channels of 1D flow. The number of particles can vary in each of the moving rows, causing most of the topological defects shown in Fig. 4(d) to align with the direction of drive and producing the anisotropic or smectic type ordering shown in $S(k)$ in the inset of Fig. 4(d). Smectic type flows of particles in periodic pinning array structures have been observed in simulations of vortices and colloidal particles moving over quasiperiodic arrays[42,44] as well as for the incommensurate flow in periodic arrays[49].

The symmetry breaking flow produces signatures in the velocity force curves $\langle V_x \rangle$ vs F_d, as shown in Fig. 5(a,b) for two states that form pinned periodic stripes, $f = 4.3$ and $f = 3.7$. Here the black line is for the initial upward sweep of F_d, and the red line is for sweeping F_d back down to zero. Neither of these fillings have a finite depinning threshold within our resolution; however, both have a two-step velocity response, which for $f = 4.3$ in Fig. 5(a) is associated with a jump up in $\langle V_x \rangle$ just above $F_d = 0.1$. In the inset of Fig. 5(a) we plot the corresponding $\langle V_y \rangle$ vs F_d where we find a linear increase in the negative y-direction velocity followed by

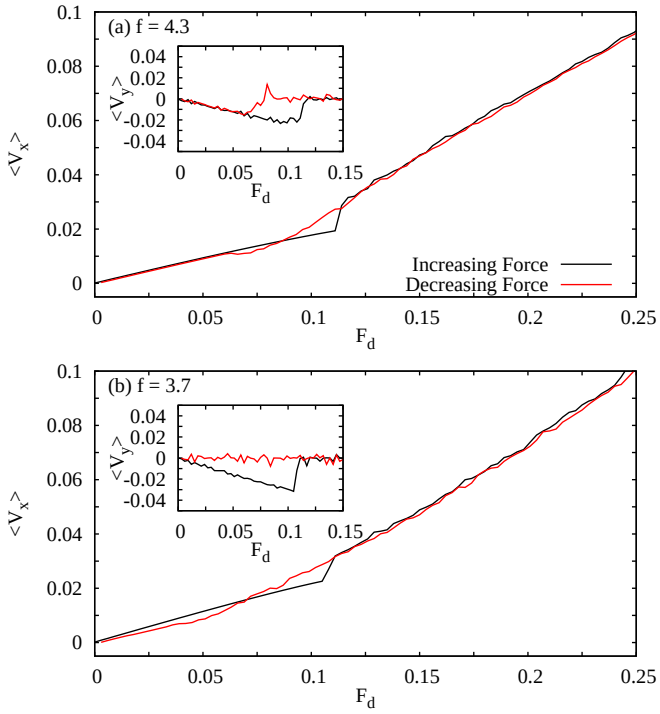

FIG. 5: The $\langle V_x\rangle$ vs F_d curves for increasing (black) and decreasing (red) sweeps of F_d at fillings that form pinned stripe states. (a) At $f = 4.3$, there is a jump up in $\langle V_x\rangle$ near $F_d = 0.1$ at the transition from stripe flow to smectic flow. Inset: the corresponding $\langle V_y\rangle$ vs F_d shows that in the stripe flow regime, the particles are also flowing in the negative y-direction, but this motion is lost at the stripe-smectic flow transition. There is hysteresis across the stripe-smectic flow transition. (b) $\langle V_x\rangle$ vs F_d for $f = 3.7$. Here the smectic flow is stable all the way down to $F_d = 0.0$. Inset: The corresponding $\langle V_y\rangle$ vs F_d.

a sharp jump into a fluctuating state with $\langle V_y\rangle = 0$ at the same value of F_d where a jump in $\langle V_x\rangle$ appears in the main panel. This feature marks the transition from symmetry breaking flow of stripes to the 1D winding smectic flow. The velocity-force curves in Fig. 5(a) and its inset also show hysteresis across the stripe-smectic flow boundary, indicating that when the external drive is reversed, the system can remain in the smectic flow state down to a drive lower than that at which the state first appeared during the increasing sweep of F_d. For $f = 3.7$, Fig. 5(b) shows that a similar set of dynamics occurs; however, in this case the smectic flow persists for the decreasing sweep of F_d all the way down to $F_d = 0.0$. In general, we observe symmetry breaking flow in regimes where stripe domain wall patterns form. Symmetry breaking flows have also been found for driven vortex systems when the vortices form effective composite objects such as dimers that possess an orientational degree of freedom[53]. This is different from the situation we observe here, where the symmetry breaking is a result of the large scale symmetric patterns that form. Symmetry breaking flow has also been observed in simulations of colloidal particles moving over egg-carton arrays in the weak substrate limit when the particles form a triangular lattice that does not have the same orientation as the substrate lattice[20]. In that case the entire lattice flows elastically. This differs from the flow shown in Fig. 4, where the motion is confined only to the grain boundaries and does not involve all the particles in the system.

In Fig. 6(a,d) we show the velocity histograms at $f = 4.3$ and $F_d = 0.05$. Here $P(v_x)$ has a positive average value with several peaks, while the corresponding $P(v_y)$ has a net negative value due to the symmetry breaking flow along the negative y-direction. The additional peaks in the distributions arise due to the highly ordered flow that occurs in this phase. The particles move in a synchronized fashion, producing a periodic velocity time series. For $F_d = 0.10$ in Fig. 6(b,e), the stripe flow occurs for the initial ramp up of the external drive; however, during the ramp down, the system remains in a smectic flow regime so that $\langle V_y\rangle = 0.0$, as seen in the symmetric distribution of $P(v_y)$ in Fig. 6(e). At $F_d = 0.35$, $P(v_x)$ in Fig. 6(c) has two prominent peaks from the pinned and flowing particles, but the additional smaller scale peaks that appeared for the symmetry breaking flow are lost since in the smectic flow regime, the different channels move at different velocities, and the resulting more disordered flow smears out the velocity distributions. The corresponding $P(v_y)$ has a symmetric profile, indicating that the flow is oriented in the x-direction. The two satellite peaks in $P(v_y)$ are due to the semi-periodic oscillations of a number of the channels, as shown in the trajectory images in Fig. 4(b). We observe a similar set of velocity distributions at $f = 3.7$ as well as at other fillings where the stripe state appears. At $f = 4.5$, the static phase does not form stripes but instead organizes into a checkerboard pattern[4]. When this pattern is driven, it transforms into a stripe phase and shows dynamics similar to those described for the $f = 4.3$ system.

IV. FLOW FROM $4.6 < f \leq 5.0$

In the range $4.6 < f < 5.0$, the static ordered stripe states are replaced by disordered patch regimes. The patches consist of regions of square ordering that grow in extent with increasing f until the entire system forms a square lattice at $f = 5.0$.[4]. The depinning threshold is finite in the patch regime; however, the velocity response is smooth as shown in Fig. 7(a) where we plot $\langle V_x\rangle$ vs F_d for $f = 4.7$. At $f = 5.0$, Fig. 7(a) shows that there is a sharp finite depinning threshold, while at $f = 4.7$ the depinning threshold occurs at a lower value of $F_d = 0.025$ and the response above depinning shows a smooth increase. The particle trajectories above depinning for $f = 4.7$, shown in Fig. 8(a) for $F_d = 0.05$, indicate that disordered winding channels of flow form, composed of localized soliton type pulses randomly dis-

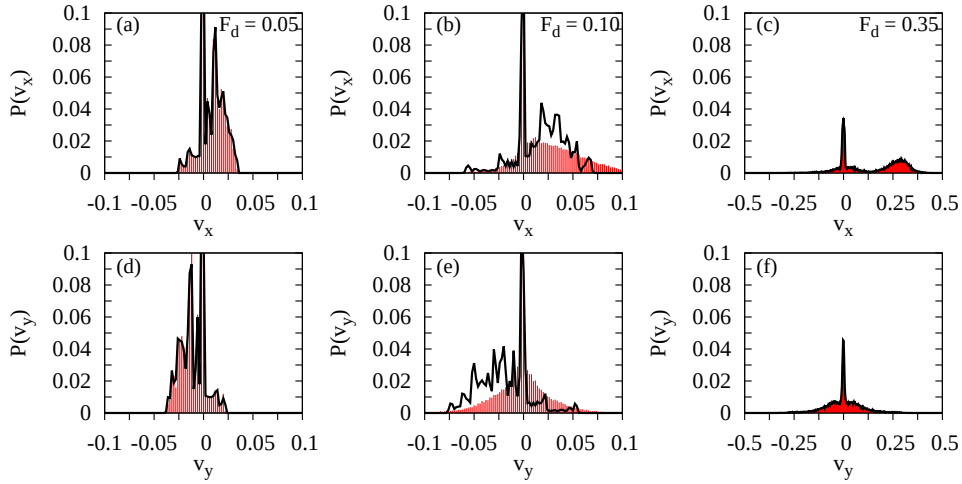

FIG. 6: The velocity histograms for $f = 4.3$. (a,b,c) $P(v_x)$; (d,e,f) $P(v_y)$. (a,d) $F_d = 0.05$. (b,e) $F_d = 0.1$. (c,e) $F_d = 0.35$. Black lines: Increasing sweep of F_d. Filled red curves: Decreasing sweep of F_d.

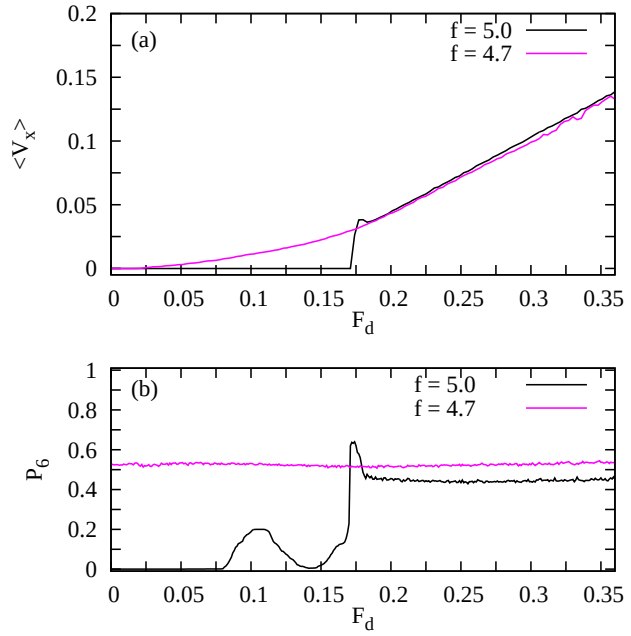

FIG. 7: (a) $\langle V_x \rangle$ vs F_d for a filling of $f = 4.7$ (black) and $f = 5.0$ (purple). (b) The corresponding P_6 vs F_d.

tributed throughout the system. At $F_d = 0.1$, shown in Fig. 8(b), these disordered regions start to proliferate. At the higher drive $F_d = 0.2$, illustrated in Fig. 8(c), the flow is more strongly disordered, while at $F_d = 0.35$, shown in Fig. 8(d), the flow starts to become more ordered and is confined into 1D winding channels in the interstitial regions. Figure 7(b) shows that P_6 vs F_d for $f = 4.7$ undergoes very little change over the range of drives examined. In contrast, for $f = 5.0$, P_6 starts off at zero since the system exhibits square ordering. Within the pinned regime, a portion of the particles are not directly trapped by the pinning sites so their positions can distort under the external drive, causing the initial pinned square order to transform under the external drive even in the absence of particle flow. This produces a peak in P_6 near $F_d = 0.1$. As F_d continues to increase, the system disorders, producing a drop in P_6 below the depinning threshold. For higher drives P_6 reaches a steady state value. For fillings above $f = 5.0$, the depinning threshold decreases and there is a two stage depinning response.

At $f = 4.7$, there is no hysteresis in the response to a drive. The velocity force characteristics for $f = 4.7$ in Fig. 7(a) can be fit to the power-law form $V \propto (F_d - F_c)^\beta$, where F_c is the critical depinning force. We find $1.5 < \beta < 2.0$, consistent with the values obtained for disordered flows in the depinning of colloidal systems driven over random substrates[50] and for vortices driven over random pinning[51]. This indicates that although the system has an underlying periodic substrate, there are certain fillings where the strong structural disorder caused by frustration effects can produce dynamics that resemble those found for systems with random substrates.

The velocity histograms $P(v_x)$ at $f = 4.7$ plotted in Fig. 9 for different values of F_d show that there is no gap between the zero velocity component peak and the higher velocity peak in the disordered flow regime, even at the higher drive of $F_d = 0.35$. The peak at higher v_x is strongly smeared. Simulations of vortices moving over random substrates produced a series of velocity histograms for increasing drive with similar characteristics[52]. For the filling at $f = 4.7$, the initial motion near $F_d = 0.05$ has a soliton or crinkle type form where pulses move through the system and individual particles move only about a lattice constant each time the pulse passes by. Unlike the more ordered fillings, the pulse motion is not strictly confined to 1D but can show considerable transverse mobility as well. The system gradually transitions to a state with a combina-

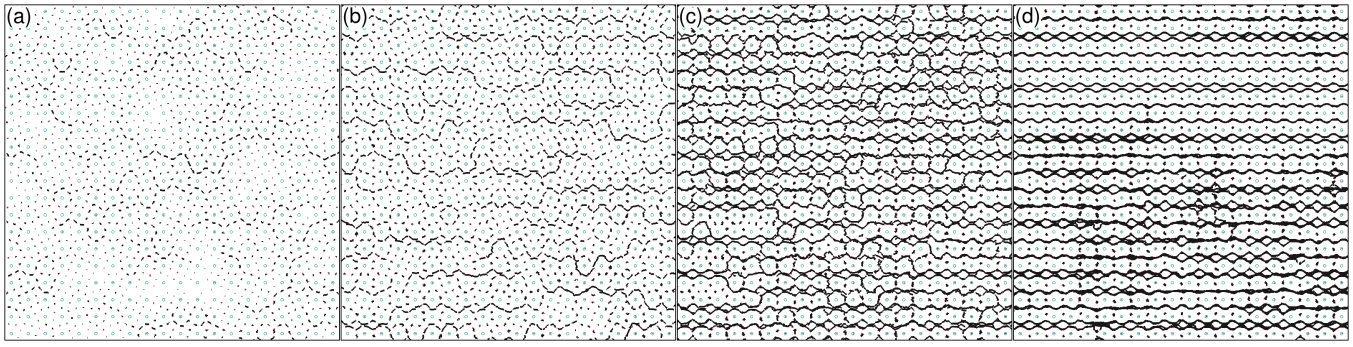

FIG. 8: The particle trajectories over a fixed time interval for the $f = 4.7$ state. (a) $F_d = 0.05$ (b) $F_d = 0.1$, (c) $F_d = 0.2$ and (d) $F_d = 0.35$.

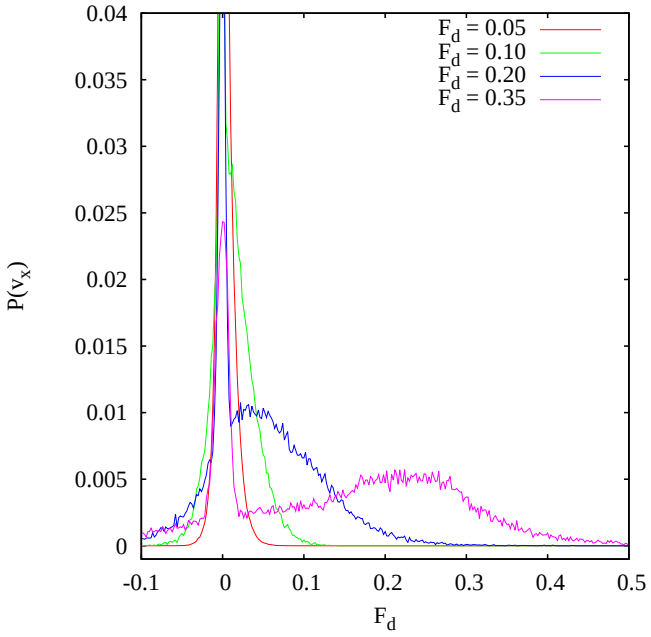

FIG. 9: The velocity histograms $P(v_x)$ for $f = 4.7$ at $F_d = 0.05$ (red), 0.1 (green), 0.2 (blue), and 0.35 (purple).

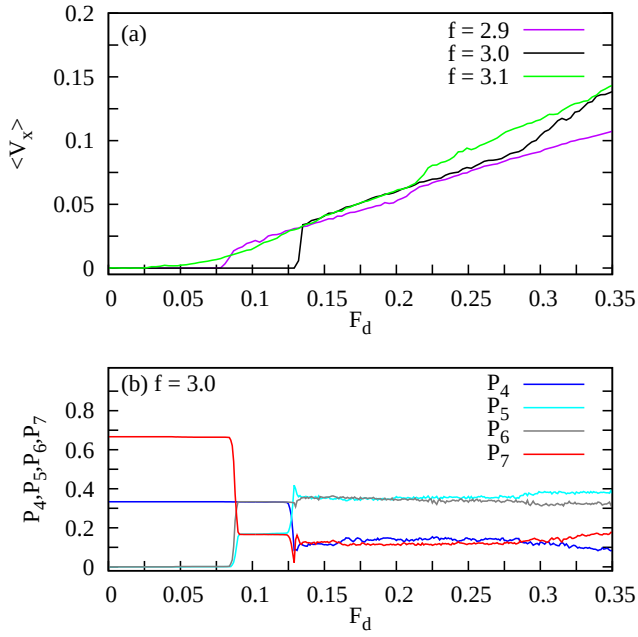

FIG. 10: (a) $\langle V_x \rangle$ vs F_d for $f = 3.0$ (highest depinning threshold), $f = 2.9$ (middle depinning threshold), and $f = 3.1$ (lowest depinning threshold). (b) P_4 (dark blue), P_5 (light blue), P_6 (gray), and P_7 (red) vs F_d for the $f = 3.0$ case. Here there is a structural transition within the pinned phase to an anisotropic lattice.

tion of soliton type motion and continuous motion near $F_d = 0.2$, while at $F_d = 0.35$ the motion is mostly continuous.

V. FLOW NEAR $f = 3.0$ AND 2.0

For fillings just above and below $f = 3.0$, the system forms grain boundaries and the dynamics are similar to those observed for the grain boundary forming states near $f = 4.0$. In Fig. 10(a) we plot $\langle V_x \rangle$ vs F_d for $f = 2.9$, 3.0, and 3.1. Here the maximum in the depinning threshold occurs for $f = 3.0$ near $F_d = 0.125$, with a lower depinning threshold for $f = 2.9$ and an even lower threshold for $f = 3.1$. In all cases there is a multiple step depinning process. The initial motion for $f = 3.1$ and $f = 2.9$ occurs via the depinning of the grain boundaries. In Fig. 10(b) we plot P_4, P_5, P_6, and P_7 for the $f = 3.0$ state. Here the ordered ground state persists up to $F_d = 0.075$, at which point the interstitially pinned particles have their positions distorted strongly enough that a new pinned structure forms. This structural transformation within the pinned state is similar to the structural transition discussed earlier for the $f = 5.0$ sample. Just above $F_d = 0.125$, depinning occurs and is accompanied by a small jump in P_n, with $n = 4$, 5, 6, 7. The structural transformation is illustrated in Fig. 11(a)

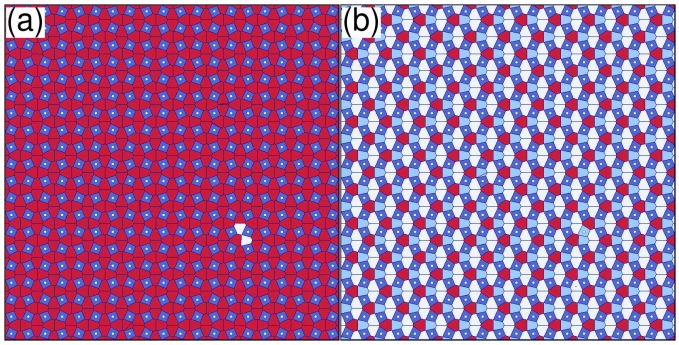

FIG. 11: The Voronoi construction (blue lines) for the $f = 3.0$ state at (a) $F_d = 0.05$, at the moment when the ground state first begins to distort (indicated by the two white polygons), and (b) $F_d = 0.1$ showing the transformed pinned structure. The Voronoi polygons are colored according to their number of sides: 4 (dark blue), 5 (light blue), 6 (white), and 7 (red).

where we plot the Voronoi construction at $F_d = 0.05$ in the ground state pinned structure at the moment when it first begins to distort noticeably, while in Fig. 11(b) we show the anisotropic pinned structure at $F_d = 0.10$.

At $f = 2.0$ the system forms a square lattice, while at $f = 1.95$ and $f = 2.05$ the incommensurate configurations do not form grain boundaries but rather isolated islands similar to the fillings just above and below $f = 1.0$. In Fig. 12(a) we plot V_x vs F_d for $f = 1.95$, 2.0, and 2.05. The highest depinning threshold occurs for $f = 2.0$, where the depinning occurs via the continuous flow of the interstitial particles while the particles at the pinning sites remain pinned. At drives higher than those shown in the figure, a second depinning transition occurs when the particles at the pinning sites become mobile. At $f = 2.05$, the interstitial depinning occurs in two steps. Above the first step, we find soliton type motion of the extra interstitial particles in the square lattice ground state, while above the second step we find the same type of depinning that occurs at $f = 2.0$ where all the interstitial particles move. For $f = 1.95$, a similar scenario occurs; however, the depinning threshold is higher than for $f = 2.05$ since for $f = 1.95$ the initial depinning is of vacancies or anti-kinks which have a higher depinning threshold than the kinks. In Fig. 12(b,c) we plot P_4 and P_6, respectively, versus F_d for the same three fillings. At $f = 2.0$ we observe a transition in the pinned state from a square lattice to a disordered lattice with sixfold ordering due to the shifting of the interstitial particles under the applied drive. This is followed by a jump into a more disordered flowing state. A similar trend occurs for the incommensurate cases with additional disorder.

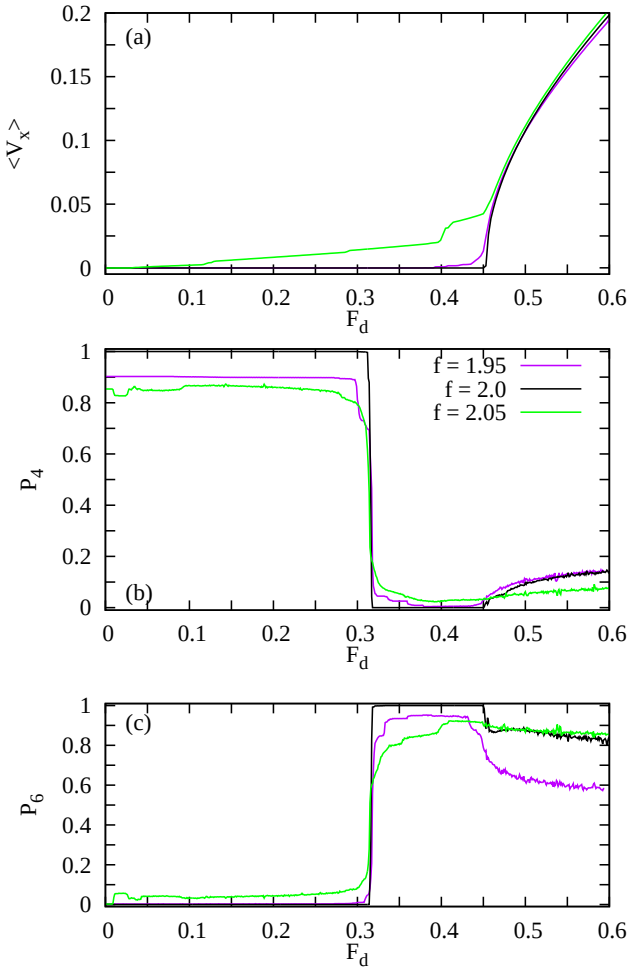

FIG. 12: (a) $\langle V_x \rangle$ vs F_d for $f = 2.0$ (highest depinning threshold) $f = 1.95$ (middle depinning threshold), and $f = 2.05$ (lowest depinning threshold). (b) The corresponding P_4 vs F_d. (c) The corresponding P_6 vs F_d.

VI. SUMMARY

We have investigated the sliding dynamics for colloidal particles on periodic two dimensional muffin-tin type pinning arrays. In the non-driven regime, this system was previously shown to exhibit pattern formation in the form of domain walls, stripes, and disordered phases at incommensurate fillings, particularly in the range $4.0 < f < 5.0$. Here we find that a rich variety of distinct dynamical phases occur in this system including domain wall dynamics as well as disordered and continuous flow phases associated with characteristic velocity distributions and structural order. Transitions between dynamic phases produce distinct features in the velocity force curves, velocity histograms, particle trajectories, and structural ordering. The system is most strongly pinned at the commensurate fillings, while at the incommensurate fillings the system is weakly pinned and undergoes multiple depinning transitions. The initial depinning occurs via soliton type motion or by the motion of domain walls. In the domain wall regime, when the domain wall depins, individual particles only move about

a lattice constant each time the domain wall moves past. For increasing drive the domain walls start to fluctuate, and at higher drives there is a transition to the continuous flow of interstitial particles when the domain wall structure breaks apart. In the regime where the domain walls form stripes, the particles move at an angle with respect to the drive above depinning, while at higher drives the stripes break apart and the particle motion is in the direction of drive. We also show that even within the pinned regimes, the external drive can induce structural transitions in the system since the interstitially pinned particles can have their positions distorted relative to the particles trapped by pinning sites. Our results on how the motion of domain walls or incommensurations leads to different dynamical responses should be general to other systems exhibiting commensurate-incommensurate transitions, such as friction on incommensurate surfaces where domain walls are present, and the flow of vortices in type-II superconductors.

Acknowledgments

This work was carried out under the auspices of the NNSA of the U.S. DoE at LANL under Contract No. DE-AC52-06NA25396. D.M. and J.A. received support from the ASC Summer Workshop program at LANL.

[1] P. Bak, Rep. Prog. Phys. **45**, 587 (1982).
[2] S.N. Coppersmith, D.S. Fisher, B.I. Halperin, P.A. Lee, and W.F. Brinkman, Phys. Rev. Lett. **46**, 549 (1981).
[3] S. Bleil, H.H. von Grünberg, J Dobnikar, R. Castañeda-Priego and C Bechinger, Europhys. Lett. **73**, 450 (2006).
[4] D. McDermott, J. Amelang, L.M. Lopatina, C.J. Olson Reichhardt, and C. Reichhardt, Soft Matter **9**, 4607 (2013).
[5] K. Harada, O. Kamimura, H. Kasai, T. Matsuda, A. Tonomura, and V.V. Moshchalkov, Science **274**, 1167 (1996).
[6] C. Reichhardt, J. Groth, C.J. Olson, S.B. Field, and F. Nori, Phys. Rev. B **54**, 16108 (1996).
[7] C. Reichhardt, C.J. Olson, and F. Nori, Phys. Rev. B **57**, 7937 (1998).
[8] J. Gutierrez, A.V. Silhanek, J. Van de Vondel, W. Gillijns, and V.V. Moshchalkov, Phys. Rev. B **80**, 140514 (2009).
[9] W.V. Pogosov, H.J. Zhao, V.R. Misko, and F.M. Peeters, Phys. Rev. B **81**, 024513 (2010).
[10] S. Avci, Z.L. Xiao, J. Hua, A. Imre, R. Divan, J. Pearson, U. Welp, W.K. Kwok, and G.W. Crabtree, Appl. Phys. Lett. **97**, 042511 (2010).
[11] S. Tung, V. Schweikhard, and E.A. Cornell, Phys. Rev. Lett. **97**, 240402 (2006); H. Pu, L.O. Baksmaty, S. Yi, and N.P. Bigelow, Phys. Rev. Lett. **94**, 190401 (2005).
[12] G. Grüner, Rev. Mod. Phys. **60**, 1129 (1988).
[13] C. Bechinger, M. Brunner, and P. Leiderer, Phys. Rev. Lett. **86**, 930 (2001).
[14] C. Reichhardt and C.J. Olson, Phys. Rev. Lett. **88**, 248301 (2002).
[15] M. Brunner and C. Bechinger, Phys. Rev. Lett. **88**, 248302 (2002).
[16] A. Libál, C. Reichhardt, and C.J. Olson Reichhardt, Phys. Rev. Lett. **97**, 228302 (2006).
[17] A. arlah, E. Frey, and T. Franosch, Phys. Rev. E **75**, 021402 (2007).
[18] S. El Shawish, J. Dobnikar, and E. Trizac, Soft Matter **4**, 1491 (2008).
[19] C. Reichhardt and C. J. Olson Reichhardt Phys. Rev. E **80**, 022401 (2009).
[20] C. Reichhardt and C.J. Olson Reichhardt, Phys. Rev. E 85, 051401 (2012).
[21] A. Vanossi, N. Manini, and E. Tosatti, Proc. Natl. Acad. Sci. **109**, 16429 (2012).
[22] P. Tierno, Soft Matter **8**, 11443 (2012).
[23] G. Coupier, M. Saint Jean, and C. Guthmann, Phys. Rev. B **75**, 224103 (2007).
[24] O.M. Braun, T. Dauxois, M.V. Paliy, and M. Peyrard, Phys. Rev. Lett. **78**, 1295 (1997).
[25] O.M. Braun, T. Dauxois, M.V. Paliy, and M. Peyrard, Phys. Rev. E **55**, 3598 (1997).
[26] O.M. Braun, M.V. Paliy, J. Röder, and A.R. Bishop, Phys. Rev. E 63, 036129 (2001).
[27] O.M. Braun and Y.S. Kivshar, *The Frenkel-Kontorova Model: Concepts, Methods, and Applications* (Springer, 2004).
[28] C.V. Achim, J.A.P. Ramos, M. Karttunen, K.R. Elder, E. Granato, T. Ala-Nissila, and S.C. Ying, Phys. Rev. E **79**, 011606 (2009).
[29] Y. Yang, W.-S. Duan, J.-M. Chen, L. Yang, J. Teki, Z.-G. Shao, and C.-L. Wang, Phys. Rev. E **82**, 051119 (2010).
[30] A. Benassi, A. Vanossi, and E. Tosatti, Nature Commun. **2**, 236 (2011).
[31] A. Vanossi, N. Manini, M. Urbakh, S. Zapperi, and E. Tosatti, Rev. Mod. Phys. **85**, 529 (2013).
[32] A. Chowdhury, B.J. Ackerson, and N.A. Clark, Phys. Rev. Lett. **55**, 833 (1985).
[33] P. Tierno, Phys. Rev. Lett. **109**, 198304 (2012).
[34] P.T. Korda, M.B. Taylor, and D.G. Grier, Phys. Rev. Lett. **89**, 128301 (2002).
[35] M.A. Tahir, L. Gao, L.N. Virgin, and B.B. Yellen, Phys. Rev. E **84**, 011403 (2011).
[36] M. Balvin, E. Sohn, T. Iracki, G. Drazer, and J. Frechette, Phys. Rev. Lett. **103**, 078301 (2009).
[37] T. Neuhaus, M. Marechal, M. Schmiedeberg, and H. Löwen, Phys. Rev. Lett. **110**, 118301 (2013).
[38] J. Hasnain, S. Jungblut, and C. Dellago, Soft Matter **9**, 5867 (2013).
[39] A. Pertsinidis and X.S. Ling, Phys. Rev. Lett. **100**, 028303 (2008).
[40] T. Bohlein, J. Mikhael, and C. Bechinger, Nature Mater. **11**, 126 (2011).
[41] M. Peyard and S.J. Aubry, J. Phys. C **16**, 1593 (1983).
[42] C. Reichhardt and C. J. Olson Reichhardt, Phys. Rev. Lett. **106**, 060603 (2011).
[43] J.A. Kromer, M. Schmiedeberg, J. Roth, and H. Stark, Phys. Rev. Lett. **108**, 218301 (2012).
[44] T. Bohlein and C. Bechinger, Phys. Rev. Lett. **109**, 058301 (2012).
[45] J. Mikhael, J. Roth, L. Helden, and C. Bechinger, Nature

454, 501 (2008).
[46] M. Schmiedeberg and H. Stark, Phys. Rev. Lett. **101**, 218302 (2008).
[47] C. Reichhardt, C.J. Olson, and F. Nori, Phys. Rev. Lett. **78**, 2648 (1997).
[48] K. Mangold, P. Leiderer, and C. Bechinger, Phys. Rev. Lett. **90**, 158302 (2003).
[49] C. Reichhardt and C.J. Olson Reichhardt, J. Phys.: Condens. Matter **25**, 225702 (2012).
[50] C. Reichhardt and C.J. Olson, Phys. Rev. Lett. **89**, 078301 (2002).
[51] S. Bhattacharya and M.J. Higgins, Phys. Rev. Lett. **70**, 2617 (1993); D. Domínguez, Phys. Rev. Lett. **72**, 3096 (1994).
[52] M.C. Faleski, M.C. Marchetti, and A.A. Middleton, Phys. Rev. B **54**, 12427 (1996).
[53] C. Reichhardt and C. J. Olson Reichhardt, Phys. Rev. B **78**, 224511 (2008).